Crystallographic effect on subsurface damage formation in silicon microcutting

Jiwang Yan [a,*], Tooru Asami [b], Hirofumi Harada [c], Tsunemoto Kuriyagawa [b]

[a] Department of Mechanical Engineering, Keio University, Yokohama, Japan
[b] Department of Mechanical Systems and Design, Tohoku University, Sendai, Japan
[c] Nano-Electronics Materials Unit, National Institute for Materials Science, Tsukuba, Japan

Submitted by Shoichi Shimada (1), Osaka Electro-Communication University, Japan

ABSTRACT

Nanoprecision plunge cutting tests were carried out on single-crystal silicon (0 0 1) samples along various directions at different tool rake angles, and subsurface damage was characterized by cross-sectional transmission electron microscopy and laser micro-Raman spectroscopy. It was found that amorphization, poly-crystallization, dislocation and internal microcracking occurred and these material responses depended strongly on the cutting direction. When cutting in the $[1\,\bar{1}\,0]$ and $[0\,\bar{1}\,0]$ directions, deep line defects consisting of microcracks and dislocation groups occurred even when the surface was "ductile"-cut; while for the $[128\,\overline{309}\,0]$ direction, the damage depth was reduced by a factor of five.

© 2012 CIRP.

1. Introduction

Single-crystal silicon is an important substrate material for solar cells, electronic devices and infrared optics. Improving subsurface integrity of silicon is crucial for manufacturing high-precision optical and electronic products [1,2]. There have been a number of studies on silicon machining, where surface damage was investigated [3,4]. However, to date, the mechanism of subsurface damage (SSD) is not well understood. Since it is difficult to directly observe SSD, molecular dynamics [5,6] has been used to simulate the cutting mechanisms; though there are very few systematic experimental investigations on SSD formation. The lack of quantitative information on SSD depth and microstructure has greatly limited the optimization of silicon machining and subsequent damage-removal processes.

In this study, nanoprecision plunge cutting tests were performed on silicon along various crystal orientations, and the SSD was examined experimentally. In plunge cutting, individual cuts can be made on pristine single-crystal silicon without preexisting defects. It is different from diamond turning [7–9], where all cuts except the first are made on a damaged substrate and not on the starting single-crystal material due to the cross feed of the tool. To directly observe the SSD, cross-sectional transmission electron microscopy (XTEM) was used first wherein samples were prepared by focused ion beam (FIB) techniques. Then, a nondestructive method based on laser Raman spectroscopy was used to quantitatively measure the SSD depth. Following our previous paper [10] where the effects of depth of cut and tool rake angle were investigated, crystallographic effects on SSD formation were specifically examined in this study. The findings of this study will provide useful guidelines for surface integrity improvements in ultraprecision machining processes.

2. Experimental procedures

Cutting tests were carried out using a four-axis (XYZB) ultraprecision lathe, which has a step resolution of 1 nm. A single-crystal diamond tool (nose radius 10 mm) was transversely fed in the X direction while the depth of cut was continuously varied in the Z direction from 0 to 1 μm at a constant cutting speed of 0.0083 m/s. The tool rake angle was changed from −15° to −45° by rotating the B-axis rotary table on which the diamond tool was fixed. Accordingly, the relief angle was changed in the range of 21°–51°. An electronic device grade n-type single-crystal silicon (0 0 1) wafer was used as the workpiece. Considering the symmetry in the lattice structure of Si (0 0 1), cutting tests were carried out in three different directions: 0°, 22.5°, and 45°, with respect to the flat orientation of the wafer. As a result, microgrooves along the $[1\,\bar{1}\,0]$, $[128\,\overline{309}\,0]$ and $[0\,\bar{1}\,0]$ directions, as schematically shown in Fig. 1, were generated precisely while other conditions were kept strictly the same. A piezoelectric dynamometer (Kistler 9256A) was used to measure the micro cutting forces during the cutting tests.

To directly observe the SSD by XTEM, FIB was used to extract XTEM samples from the bottom of the plunge-cut microgrooves (Fig. 1). The sample thickness was reduced to ~100 nm to enable electron transmission in the XTEM. In order to protect the sample from possible damage from the FIB, carbon (C) and tungsten (W) coatings were deposited on top of the samples. A laser micro-Raman spectrometer was then used to characterize the samples and the SSD depth was measured by calculating the Raman intensity ratio [11]. The laser in the Raman system had a wavelength of 532 nm, and in turn, produced a penetration depth of ~1 μm into the silicon substrate. The laser spot size was 1 μm, thus enabling the test points to be precisely located at any region within the microgroove.
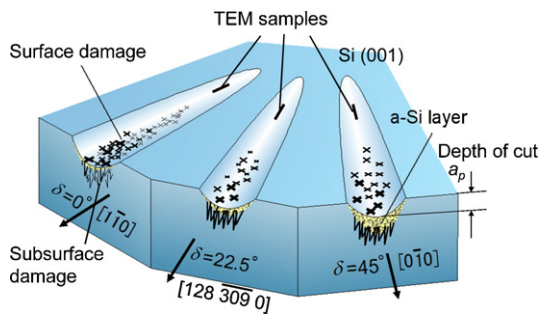
* Corresponding author.

Fig. 1. Schematic of plunge-cut microgrooves and locations of TEM sample extraction.

Fig. 3. Variation in the critical depth of cut as a function of cutting direction angle and tool rake angle.

3. Results and discussion

3.1. Crystallographic effect on surface damage threshold

First, surface damage on the specimens was observed for comparison with the SSD. Fig. 2 shows the Nomarski micrographs of microgrooves cut along different directions at a tool rake angle of −30°. From right to left, as the depth of cut increased, the microgrooves gradually broadened and became deeper. At a critical depth of cut, microcracks begin to form, and the density of the microcracks increases with the depth of cut. A clear brittle-ductile transition boundary can be identified on the groove surface. Fig. 3 shows the change in the critical depth of the cut where the brittle-ductile transition occurred, as a function of cutting direction and tool rake angle. Five cuts were made for each tool rake angle, and the average critical depth of cut is plotted. The results indicate that a moderately negative rake angle (−30°) is helpful for obtaining a ductile-cut surface. Among the three cutting directions, the 22.5° direction had the highest ductile machinability.

3.2. Crystallographic effect on subsurface microstructure

XTEM samples were extracted from the groove bottoms where the depth of cut was 100 nm. The tool rake angle used for preparing the XTEM samples was −30°. At a cut depth of 100 nm, as seen in Fig. 3, all the grooves were ductile-cut and no damage was seen on the surface. Fig. 4(a) shows an XTEM micrograph of a sample cut in the 0° direction. Similar to previous results [10], a thin grey layer (amorphous silicon, a-Si) formed just beneath the ductile-cut surface. The average thickness of the a-Si layer was ~20 nm, which is remarkably smaller than that formed at −45° and −60° tool rake angles (~100 nm) [10]. Below the a-Si layer, there is a strained layer with dark contours. Distinctly different from previous results, many line defects are present and extend into the bulk (single-crystal silicon, c-Si) with curling. These line defects grow to a maximum depth of ~800 nm, far deeper than the depth of cut (100 nm). Fig. 4(b) shows a pair of closeup views (left: bright field; right: dark field) of the line defects. It can be seen that the upper parts of the line defects are microcracks, which are generated along
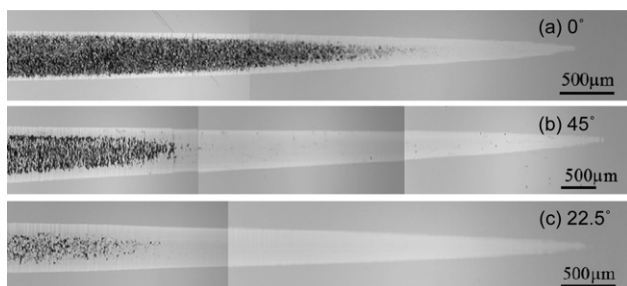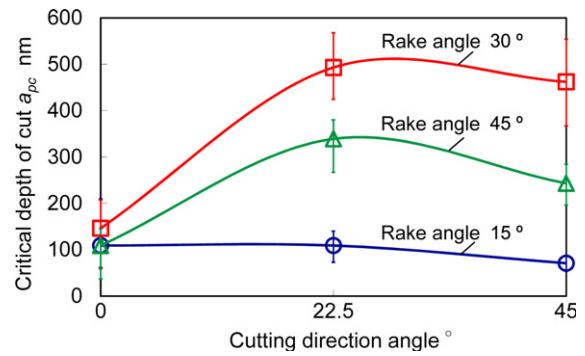
the {1 1 0} planes (35.3° from the cut surface) and {1 1 1} planes (54.7°). After the microcracks stopped propagating, very long dislocation groups were initiated at the ends of the microcracks. These dislocation groups include both edge and screw dislocations. Since the dislocation groups extend deeply into the crystalline bulk region, they significantly increase the SSD depth. Such deeply extending line defects were not observed when the depth of cut was smaller (~30 nm) or when the tool rake angle was highly negative (~45°).

Fig. 5(a) shows an XTEM micrograph of a sample cut in the 45° direction. Similar to Fig. 4(a), a thin a-Si layer is generated on the top, below which is a strained layer with curling line defects extending downwards. In Fig. 5(a), the a-Si layer was ~30 nm thick, slightly thicker than in Fig. 4(a). Clearly, the number of the line defects is fewer than in Fig. 4(a), though the maximum depth of the line defects is slightly greater than in Fig. 4(a). In this case, the line defects extend to approximately 1 μm, ten times the depth of cut. Fig. 5(b) shows a pair of closeup views of the line defects in bright and dark fields. Similar to Fig. 4(b), the shallower line defects are microcracks initiated along {1 1 0} planes (45° from the cut surface) and {1 1 1} planes (60°). When a microcrack stops propagating, dislocation groups form at the crack end. In Fig. 5(b), the strained layer contains many poly-crystalline grains (p-Si) surrounded by a-Si and microcracks.
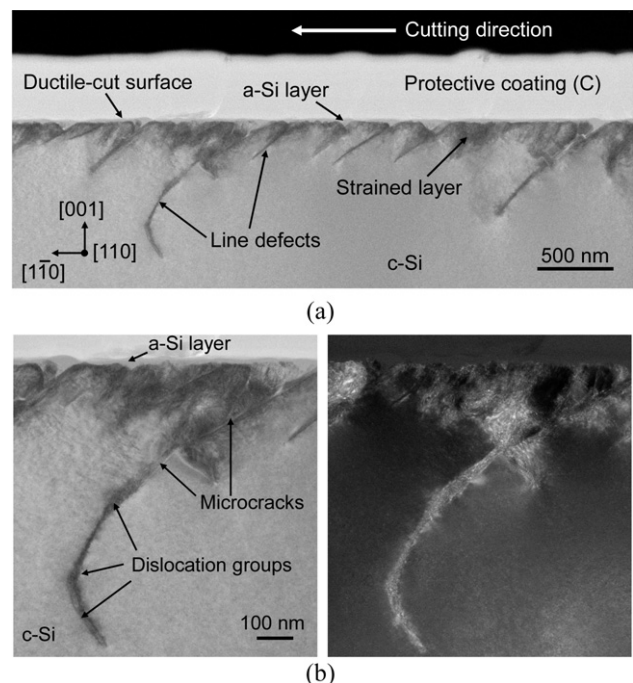

Fig. 2. Micrographs of microgrooves cut in different directions.

(a)

(b)

Fig. 4. XTEM micrographs of a sample cut along the 0° direction: (a) general view, (b) closeup bright and dark field views.
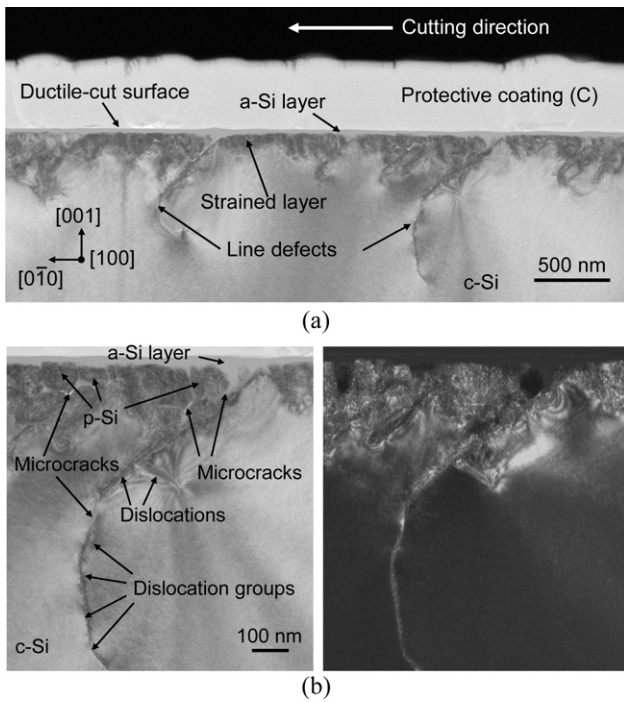
Fig. 5. XTEM micrographs of a sample cut along the 45° direction: (a) general view, (b) closeup views in bright and dark fields.

Fig. 6(a) shows an XTEM micrograph of a sample cut in the 22.5° direction. In this case, the a-Si layer is extremely thin and can barely be seen at this magnification. Compared with Figs. 4(a) and 5(a), the line defects are distinctly shorter (~200 nm) and straighter. Fig. 6(b) shows closeup views of the line defects. In this case, the microcracks were all initiated along the {1 1 1} planes (55.8° from the cut surface), while no cracks were formed along {1 1 0} planes (30.4°). Similar to Figs. 4(b) and 5(b), dislocations are seen at the ends of the microcracks.

It is also noteworthy that for all the XTEM results, there is synchronization among the a-Si layer thickness, surface
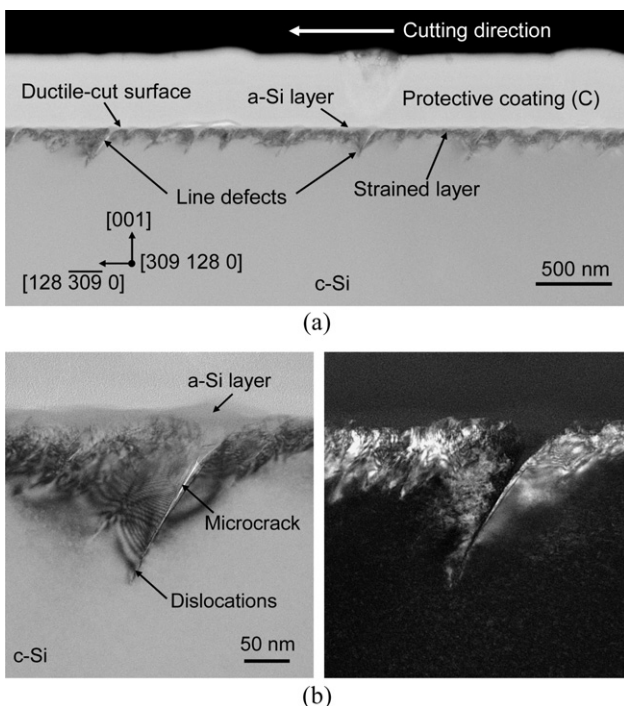

Fig. 6. XTEM micrographs of a sample cut along the 22.5° direction: (a) general view, (b) closeup views in bright and dark fields.
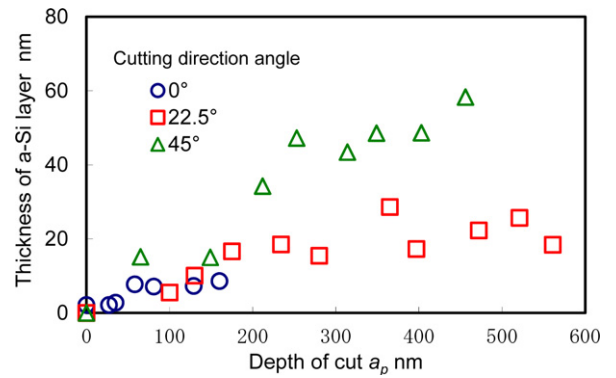

Fig. 7. Variation in a-Si layer thickness with depth of cut for different cutting directions, measured by laser micro-Raman.

waviness and microcrack generation. Near surface peaks, the a-Si layer is locally thicker and pressed into the microcracks. This phenomenon may result from unstable tool–workpiece interaction, such as stick slip. Due to micro impacts, a thicker a-Si layer is formed that protrudes into microcracks under high pressure.

3.3. Crystallographic effect on amorphization depth

To measure the depth of the a-Si layer over a wide range of cutting conditions, laser micro-Raman tests were conducted in the ductile-cut regions of the microgrooves. In the typical Raman spectra of machined silicon [11], there are two characteristic peaks: a sharp peak at 520 cm^{-1} and a broadband peak centered at 470 cm^{-1}. In order to quantitatively measure the depth of the a-Si layer, we adopted a new parameter, the Raman intensity ratio r [11]. r is the ratio of the total Raman intensities of a-Si and c-Si, obtained by integrating the Gauss- and Lorenz-fitted curves of the a-Si and c-Si peaks, respectively, with respect to the Raman shift. By calculating r, the a-Si depth can be estimated without contact and nondestructively. Fig. 7 shows the variation in the a-Si layer thickness with depth of cut for different cutting directions. For each cutting direction, the a-Si layer thickness increased gradually with the depth of cut. As a general trend, the a-Si layer is thickest in the 45° direction and thinnest in the 22.5° direction, consistent with the XTEM results in Figs. 4–6.

3.4. Crystallographic effect on micro cutting force

Fig. 8 shows plots of the resultant cutting forces as a function of depth of cut for different cutting directions. In ductile-cut regions, the force is lowest in the 22.5° cutting direction, which is the easiest direction for ductile cutting (Fig. 3), and is highest in the 0° direction which has the lowest ductile machinability. The increasing rate of the cutting force drops sharply in the 0° direction when the depth of cut increases over 300 nm. This might
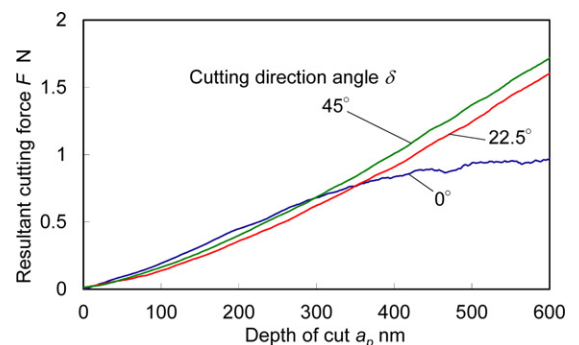

Fig. 8. Variation in cutting force with depth of cut in different cutting directions.
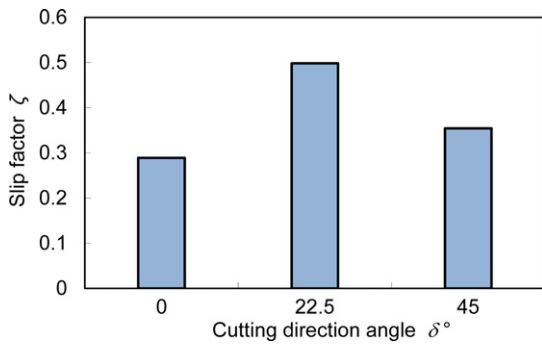
Fig. 9. Variation of slip factor with cutting direction.

be caused by the significance number of microcrack generation in this direction.

3.5. Discussion on SSD formation mechanism

Stress in silicon may be released by the following material responses: phase transition (amorphization/poly-crystallization), dislocation formation, and crack initiation. Just beneath/ ahead of the tool tip, an extremely high pressure (compressive stress) is generated [10], which causes phase transitions. As the tool tip advances into the workpiece, silicon transforms from a diamond cubic structure (Si-I) into a metallic phase (Si-II) which is sufficiently ductile to facilitate plastic flow. After the tool has passed, Si-II does not transform back into Si-I, but rather changes into an amorphous phase. For this reason, a thin a-Si layer will always be formed on top of the workpiece surface. Beyond the phase transition region, the pressure drops sharply, and shear stress and tensile stress become dominant. For silicon, dislocations are initiated by the shear stress acting on the {1 1 1} ⟨1 1 0⟩ slip system, and microcracks are generated by the tensile stress acting on the {1 1 1} (primary) or {1 1 0} (secondary) cleavage planes. When a microcrack is initiated, it extends deeply into the bulk. After the microcrack stops propagating, significant stress concentration will occur around the crack tip, inducing deep dislocation groups. A few line defects might also contain crystalline phase transition bands as shown in the MD simulation [5], though it was difficult to directly observe them in this study.

In order to reduce the depth of SSD, it is essential to prevent internal crack initiation. For a specific crystal orientation, the ease of microcracking is in reverse proportion to that for slip deformation. The ease of slip deformation is indicated by the slip factor ζ, which is based on the Schmid factor with consideration of the symmetry in slip systems [7]. Fig. 9 shows the change in ζ with cutting direction. It is clear that ζ is highest in the 22.5° direction, and lowest in the 0° direction. This trend is in reverse relation to the degree of microcracking seen in Figs. 4–6, and thus the slip factor ζ may be used as an index when selecting cutting directions for low SSD. For all cutting directions, however, a highly negative tool rake angle and/or a small depth of cut are beneficial for suppressing internal microcracks.

4. Conclusions

Nanoprecision plunge cutting tests were performed on Si (0 0 1) along various directions, and the crystallographic effects on SSD were examined. The following conclusions were obtained.

(1) SSD involves four kinds of material responses: amorphization, poly-crystallization, microcracking, and dislocation formation.
(2) Subsurface microcracks form earlier than surface microcracks in plunge cutting. Internal microcracks may exist beneath an external "ductile"-cut surface.
(3) Internal microcracks occur in the {1 1 1} and {1 1 0} planes.
(4) Internal microcracks can be reduced using a highly negative tool rake angle (∼−45°) or a small depth of cut (∼30 nm).
(5) The depth and microstructure of SSD depend strongly on the cutting direction. In the [1 1̄ 0] and [0 1̄ 0] directions, line defects including microcracks and dislocation groups form and extend to a depth of about ten times the depth of cut.
(6) Cutting in the [128 30̄9̄ 0] direction yields the best ductile machinability and the lowest SSD. The maximum damage depth is reduced by a factor of five.

The above findings may serve as references for optimizing machining conditions in silicon cutting/grinding processes.

Finally, it should be pointed out that the cutting tests in this study were performed at a constant speed (0.0083 m/s). Cutting speed may affect the thermal and dynamical aspects of a cutting process, and in turn, change SSD formation mechanism [12]. This issue is still under further investigation.

References

[1] Lucca DA, Brinksmeier E, Goch G (1998) Progress in Assessing Surface and Subsurface Integrity. Annals of the CIRP 47(2):669–693.
[2] Jawahir IS, Brinksmeier E, Saoubi RM, Aspinwall DK, Outeiro JC, Meyer D, Umbrello D, Jayal AD (2011) Surface Integrity in Material Removal Processes: Recent Advances. Annals of the CIRP 60(2):603–626.
[3] Nakasuji T, Kodera S, Hara S, Matsunaga H, Ikawa N, Shimada S (1990) Diamond Turning of Brittle Materials for Optical Components. Annals of the CIRP 39(1):89–92.
[4] Shimada S, Ikawa N, Inamura T, Takezawa N, Ohmori H, Sata T (1995) Brittle-Ductile Transition Phenomena in Microindentation and Micromachining. Annals of the CIRP 44(1):523–526.
[5] Tanaka H, Shimada S, Anthony L (2007) Requirements for Ductile-mode Machining Based on Deformation Analysis of Mono-crystalline Silicon by Molecular Dynamics Simulation. Annals of the CIRP 56(1):53–56.
[6] Inamura T, Shimada S, Takezawa N, Ikawa N (1999) Crack Initiation in Machining Monocrystalline Silicon. Annals of the CIRP 48(1):81–84.
[7] Shibata T, Fujii S, Makino E, Ikeda M (1996) Ductile-regime Turning Mechanism of Single-crystal Silicon. Precision Engineering 18(2–3):129–137.
[8] Puttick KE, Whitmore LC, Chao CL, Gee AE (1994) Transmission Electron Microscopy of Nanomachined Silicon Crystals. Philosophical Magazine A 69(1):91–103.
[9] Kunz RR, Clark HR, Nitshin PM, Rothschild M, Ahern BS (1996) High Resolution Studies of Crystalline Damage Induced by Lapping and Single-Point Diamond Machining of Si (1 0 0). Journal of Materials Research 11:1228–1237.
[10] Yan J, Asami T, Harada H, Kuriyagawa T (2009) Fundamental Investigation of Subsurface Damage in Single Crystalline Silicon Caused by Diamond Machining. Precision Engineering 33(4):378–386.
[11] Yan J, Asami T, Kuriyagawa T (2008) Nondestructive Measurement of Machining-induced Amorphous Layers in Single-crystal Silicon by Laser Micro-Raman Spectroscopy. Precision Engineering 32(3):186–195.
[12] Neugebauer R, Bouzakis KD, Denkena B, Klocke F, Sterzing A, Tekkaya AE, Wertheim R (2011) Velocity Effects in Metal Forming and Machining Processes. Annals of the CIRP 60(2):627–650.